Bending Properties of Al-Steel and Steel-Steel Composite Metal Foams

JUDITH A. BROWN, LAKSHMI J. VENDRA, and AFSANEH RABIEI

The performance of new composite metal foams (CMFs) under bending was evaluated with simultaneous acoustic emission (AE) monitoring on samples processed by cast and powder metallurgy (PM) techniques. The results showed high maximum strength in all samples up to 86 MPa with more ductile failure in PM samples. Acoustic emission behavior confirmed that the dominating failure mechanism of cast CMF is the brittle fracture of intermetallic phases that mostly exist at the interface of the steel spheres with the aluminum matrix, whereas in PM samples (100 pct steel), the failure is governed by the propagation of preexisting microporosities in the matrix resulting in a complete ductile failure. SEM imaging of the fracture surfaces supported these findings.

DOI: 10.1007/s11661-010-0343-y

I. INTRODUCTION

METAL foams are porous materials with unique combinations of thermal, mechanical, acoustic, and electrical properties desirable in many engineering applications. High stiffness-to-weight ratios and the ability to absorb large amounts of energy at relatively constant stress levels make closed cell metal foams attractive materials for automobile structural parts and crumple zones as well as structural parts for aircraft and spacecraft, where minimizing weight without sacrificing material performance is a priority.[1] Additional applications include components for vibration and acoustic damping, blast protection, boat decks and bulkheads, and prosthetic parts for biomedical applications.[1] Because the melting point of metal foam is similar to its parent material, metal foams can also be used in high-temperature and harsh environments that are unsuitable for other types of foam, such as polymer foams.[2]

Although metal foams could provide significant improvements to these applications, most current processing methods produce foams with significant variations in cell size and shape, which makes an accurate prediction of mechanical properties difficult and the performance of the foam less than desirable.[2] Strong variations in the cell structure such as missing cell walls, wiggles in the cell wall, and anisotropic cell sizes cause localized deformation bands mostly around large or highly elliptical cells and limit the performance of the whole material to a function of the strength at its weakest point.[3,4] Several studies of commercially available closed-cell Al foams show that a large number of such defects are distributed inherently throughout the material, which causes significant reductions in stiffness and strength from those predicted by scaling laws.[5–7]

This problem is solved partially by constructing metal foam from preformed hollow spheres, such as those created at Georgia Tech[8] and the Fraunhofer Institute.[9] Because the hollow spheres possess uniform cell size, shape, and wall thickness, they can produce metal foams with more uniform deformation patterns. However, because of the small point contacts between the sphere walls to support the foam structure under load, this type of hollow sphere foam exhibits low strength and low energy absorption capability.

Composite metal foam (CMF) is a new type of metal foam that addresses these issues by filling the interstitial spaces between a random dense arrangement of hollow spheres with a metallic matrix. The hollow spheres provide a known uniform cell size and shape, whereas the presence of a ductile matrix between the spheres promotes better bonding between the spheres as well as reinforces the thin cell walls, which results in higher strength and energy absorption capabilities. CMF is produced by both casting and powder metallurgy techniques and has been tested extensively in monotonic compression, loading-unloading compression, and compression-compression fatigue, showing significant improvement over the performance of existing metal foams.[10–17] In addition, a water cooling method has been developed to optimize the microstructural characteristics and mechanical properties of the foam processed by casting methods.[18]

This article reports the failure analysis of CMFs processed by both air- and water-cooled casting as well as powder metallurgy techniques under bending using *in situ* acoustic emission analysis during loading. Acoustic emission (AE) is the phenomenon of a rapid energy

JUDITH A. BROWN, Ph.D. Candidate, is with the Department of Mechanical and Aerospace Engineering, North Carolina State University, 911 Oval Drive -3250 EB III, Raleigh, NC 27695-7910. LAKSHMI J. VENDRA, formerly Ph.D. Candidate, Department of Mechanical and Aerospace Engineering, North Carolina State University, is now Mechanical Engineer IV, Baker Hughes, Houston, TX 77073. AFSANEH RABIEI, Associate Professor, is with the Department of Mechanical and Aerospace Engineering, North Carolina State University and Associate Faculty in the Department of Biomedical Engineering, North Carolina State University. Contact e-mail: arabiei@ncsu.edu

Manuscript submitted September 9, 2009.
Article published online July 1, 2010

release that generates transient elastic waves that travel through the sample and can be detected by piezoelectric sensors on the material surface when the material is subjected to a load.[19] The attributes of these waves, such as emission rate, wave frequency, peak amplitude, and wave energy, can be used to characterize material properties and to determine the location of the AE sources.[19] The material strength, strain rate, isotropy, and general failure mechanisms, as well as the presence of any defects, affect the acoustic emission signals.[19] If the fracture mechanisms of the material are known, then it can be possible to correlate the AE signals to a particular physical or mechanical process during loading and provide insight into the failure analysis of the material.[19]

II. EXPERIMENTAL TECHNIQUES

A. *Materials and Sample Processing Methods*

The hollow spheres used to produce the samples of CMFs are produced by a powder metallurgy process at the Fraunhofer Institute in Dresden, Germany.[9] Both 316L stainless steel (SS) and low carbon (LC) steel spheres are used. For both processing methods, the ratio of sphere wall thickness to sphere outer diameter is selected to be similar so that the mechanical properties of the resulting samples are comparable.

The cast samples require sphere and matrix materials with two distinctly different melting points to avoid melting of the spheres during casting when in contact with the molten matrix. The matrix material used is aluminum A356 casting alloy (Al-7 pct Si) to produce the Al-SS and Al-LC steel composite foams. All spheres used for the casting samples have an outer diameter of 3.7 mm, a wall thickness of 0.2 mm, and wall porosity of 7 pct to 8 pct. For the casting process, the spheres are placed inside a cylindrical casting mold and held in place with a wire screen. The spheres and mold are preheated in a 3300 series high-temperature laboratory furnace (CM Furnaces, Inc., Bloomfield, NJ) up to 973 K (700 °C) while the aluminum is melted simultaneously in a graphite crucible. The aluminum is cast into the mold, and the sample is either air cooled or water cooled before being removed from the mold. More details of the casting procedure are available elsewhere.[12–18]

The samples processed by powder metallurgy methods use similar sphere and matrix materials because no difference in melting point is needed for this processing method. Powder metallurgy LC steel CMF is produced from LC steel spheres with an outer diameter of 2.0 mm, wall thickness of 0.1 mm, and wall porosity of about 5 pct with Ancorsteel-1000 LC steel powder (Hoeganaes Corporation, Cinnaminson, NJ) mixed with 0.8 pct graphite as the matrix. The graphite is added for added strength and shrinkage control in the matrix for the LC steel foam. Powder metallurgy SS CMF is produced with 316L SS spheres of 2.0 mm outer diameter, 0.1 mm wall thickness, and wall porosity ranging from 6 pct to 15 pct with 316L SS powder as the matrix (no other additions). The spheres and matrix powder are placed into a square mold and vibrated to achieve a dense packing configuration and then processed through a sintering cycle in a Centorr 600-4X6W4-26HP vacuum hot press (Centorr Vacuum Industries, Nashua, NH). Details of the powder metallurgy processing method can be found elsewhere.[11–13,15]

B. *Sample Preparation*

The CMF samples were cut into thin slices for the bending tests using a Buehler Isomet 4000 linear precision saw (Buehler, Lake Bluff, IL) equipped with a 20-cm diamond wafering blade rotating at 2050 rpm and a feed rate of 1.5 mm/min. A sample thickness of about 4 mm was selected to cover at least one layer of spheres in the sample and matching the diameter of the AE sensor to maximize the sensor's sensitivity and avoid reflecting signals. This sizing of the sample thickness to be roughly the same as the diameter of the AE sensors allows for most of the AE signals to arrive at the sensor at incidence angles close to perpendicular.[20] Table I shows the composition of samples tested with their respective dimensions and relative densities.

The samples were mounted onto a sample holder using hot wax, followed by grinding and polishing on a MA-200D Automatic Lapping Polishing Machine (Musasino Denshi Corporation, Tokyo, Japan) rotating at 100 rpm. Both faces of the sample were polished with 200 and 400 grit sandpapers and 30 μ Hyprez 30-std diamond slurry (Engis Corporation, Wheeling, IL) to ensure even thickness of the sample and to reduce friction between the sample and the bending jig rollers during testing.

C. *Bending Test Procedures*

Four-point bending tests for three samples of each processing method were performed on an Autograph Shimadzu AG-5000C testing machine (Shimadzu

Table I. Composition, Processing Method, and Dimensions of Samples Tested Under 4-Point Bending

	Casting			Powder Metallurgy	
Matrix material	Aluminum alloy (A356)			316L SS	LC steel
Sphere material	316L SS	316L SS	LC steel	316L SS	LC steel
Cooling method	Air	Water	Air	Furnace	Furnace
Sphere diameter (mm)	3.7	3.7	3.7	2.0	2.0
Sphere wall thickness (mm)	0.2	0.2	0.2	0.1	0.1
Sample dimensions (mm)	60.0 × 26.9 × 3.7	53.8 × 27.6 × 3.6	59.4 × 28.9 × 3.9	48.2 × 21.0 × 2.9	59.8 × 20.5 × 2.6
Measured density (g/cm^3)	2.44	2.43	2.45	2.90	2.81
Relative density (pct)	42.1	42.0	42.3	37.5	36.3

Corporation, Kyoto, Japan) using an inner span of 10 mm and an outer span of 30 mm. Four-point bending was used to allow easy distinction between any noises caused by friction between the sample and the rollers and the useful AE signals generated by deformation mechanisms occurring in the center of the sample. The tests were conducted at room temperature, and all rollers were wrapped in Teflon tape to reduce noise caused by friction. A loading rate of 0.1 mm/min (4.50×10^{-4} strain/s) was chosen to match the strain rates used for previous monotonic compression tests (~4.5×10^{-4} strain/s). This loading rate also facilitates the detection of individual AE events without saturating the sensors while minimizing the potential for noises caused by sample shifting between the jigs. Data from the 5-kN load cell was sent through a load amplifier with a gain of 1 kN/V and recorded on a local computer using the *Waveshot! 2000* software (Keyence Corp., Osaka, Japan).

Four-channel AE monitoring through the continuous wave memory (CWM) system was used to record AE events occurring during the bending test. More information regarding this technique can be found elsewhere.[21] Two AE sensors were attached to the left and right edges of the sample in a position with as much contact between the sensor and the matrix as possible. A fast-drying glue was applied to the sensor surface and the sensor was then pressed against the sample for approximately 30 seconds until the glue had set. For each test, the sensors were mounted on the same side of the sample (left side: channels 1 and 2, right side: channels 3 and 4) and connected to the same monitoring channel for consistency in comparing data between tests. This setup is illustrated in Figure 1. The sensors were calibrated before each test by breaking a pencil lead against the specimen surface.[22]

Acoustic emission signals in the loaded samples were detected and converted to electrical signals by M 304 series piezoelectric AE sensors (Fuji Ceramics Corp., Shizuoka, Japan) of 4 mm diameter, sent through a preamplifier (A1002, Fuji Ceramics Corp.) to increase the voltage level, and recorded by the CWM computer unit. The preamplifiers were set in calibration mode, and the CWM system was set to record all events with amplitude above a detection threshold level of 30 mV.

The fracture surfaces of each sample were observed after the bending tests using a Hitachi S-3200N environmental scanning electron microscope (SEM) (Hitachi High-Technologies America, Inc., Schaumburg, IL). To prevent electron charge up on the aluminum matrix, cast samples were observed in the N-SEM mode using a Robinson Detector with an accelerating voltage of 30 kV, whereas the powder metallurgy samples were observed in high vacuum mode with an accelerating voltage of 20 kV.

III. RESULTS AND DISCUSSION

The stress-displacement curves and corresponding acoustic emission activity for each type of sample under 4-point bending tests are shown in Figure 2. The stresses reported are the maximum stresses occurring in the sample and were calculated from load cell measurements using the classic beam theory relationship for 4-point bending shown in Eq. [1].

$$\sigma = \frac{3P(L-l)}{2wt^2} \qquad [1]$$

The input parameters for Eq. [1] are load (P), inner span (l), outer span (L), and the sample cross-sectional width (w) and sample thickness (t).

The amplitude of each AE event is plotted at the crosshead displacement position where it occurred in addition to the corresponding stress and cumulative number of events per cross-sectional area that had occurred up to that point. The number of AE events observed in each sample was normalized by that sample's cross-sectional area to account for small differences in sample size. Yield stress during bending tests was determined using the 0.2 pct offset method and is presented as the average of three samples tested for each CMF processed through various routes in Figure 3. Variations in performance can be observed between the sample types, but all samples had a peak stress greater than 50 MPa with corresponding strength to density ratios of at least 20 MPa/(g/cc). These values are significantly higher than the bending strength reported for other closed-cell metal foams for use as structural materials.[1,23] Acoustic emission events observed during the bending tests reflected distinctly different behavior

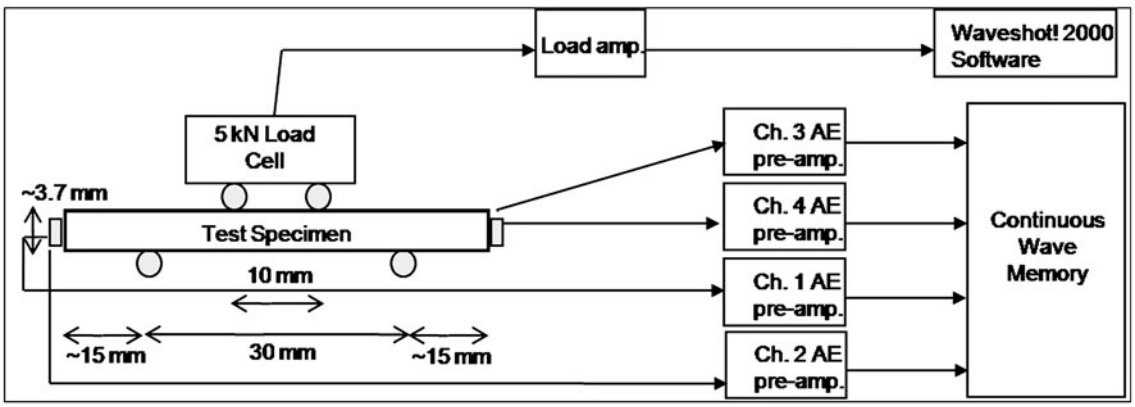

Fig. 1—Four-point bending test set up with AE monitoring.

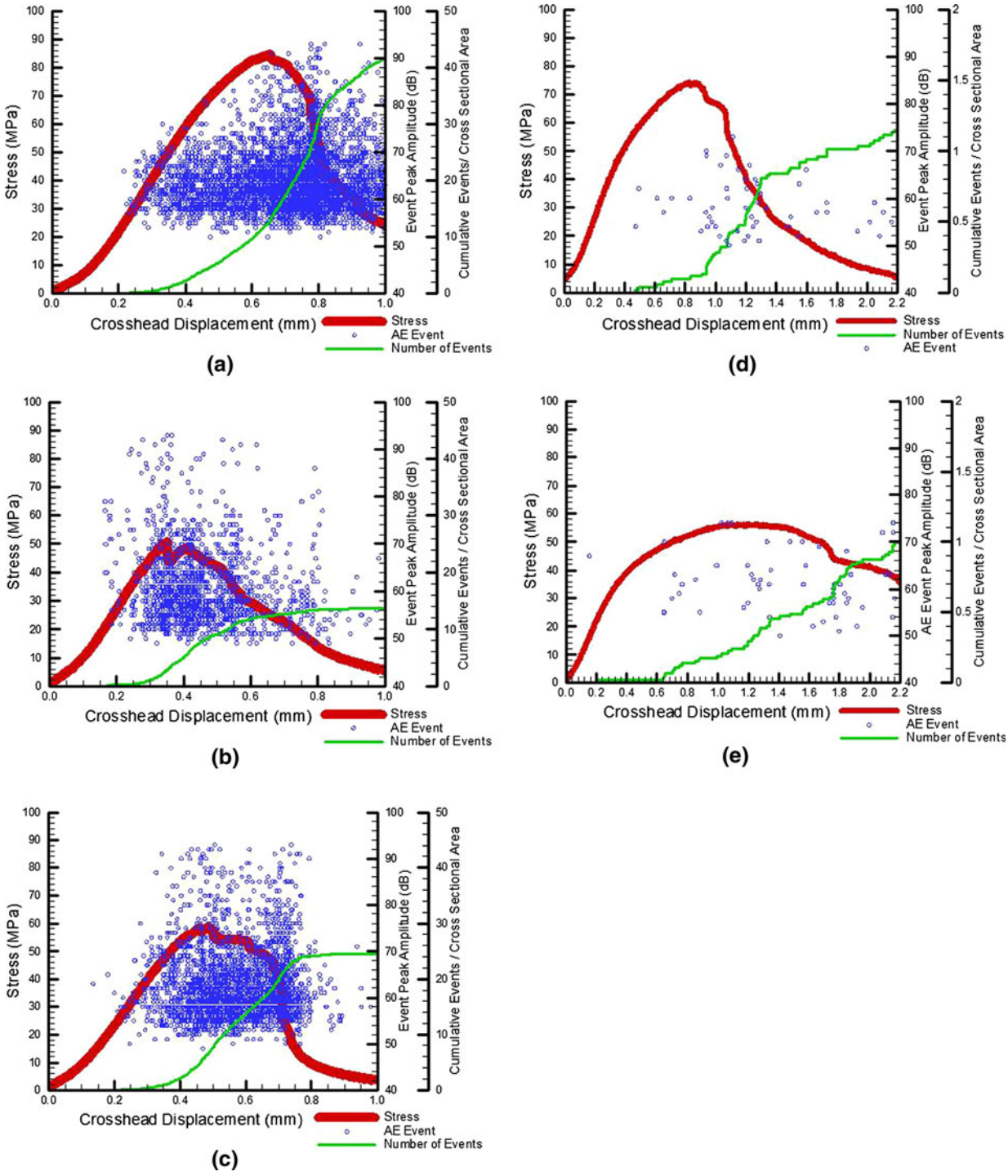

Fig. 2—AE behavior of CMF samples under 4-point bending: (*a*) Al-LC steel air cooled, (*b*) Al-SS air cooled, (*c*) Al-SS water cooled, (*d*) PMLC steel, and (*e*) PMSS.

between the powder metallurgy and the cast samples, and the effects of processing route and microstructure on the failure behavior is discussed in detail.

A. *Cast Samples*

Because of the use of dissimilar sphere and matrix materials, the samples processed by casting method contain intermetallic compounds present within the matrix and around the hollow spheres. These intermetallics form during cooling as atoms interdiffuse between the steel spheres and aluminum matrix and are brittle in nature. A previous study of the cast sample microstructure found three ternary phases present: a brittle layer at the interface between the spheres and matrix, a plate-shaped phase surrounding the outer edges of this

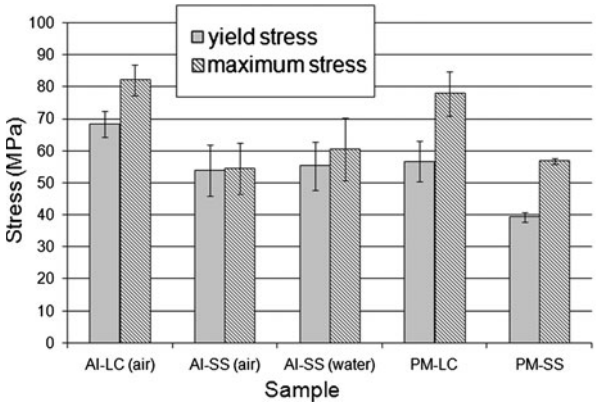

Fig. 3—Yield stress and maximum stress values of CMF samples under 4-point bending.

interface layer, and a needle-shaped phase distributed throughout the matrix.[10] As the result, to minimize the percentage of brittle intermetallic phases in cast samples, a series of water-cooled samples were processed and tested to compare the effect of those intermetallics on the properties of cast CMFs. The composition, size, and distribution of these intermetallic compounds within the microstructure have been found to govern the failure mechanisms and the type of acoustic emission released from cast samples under loading.

Figure 4 shows SEM images of cast air-cooled Al-LC steel composite foams with the distribution of intermetallic phases in the microstructure (Figure 4(a)) and its fracture surface after complete failure under bending (Figure 4(b)). Figure 5 shows SEM images of the matching fracture surfaces of an Al-SS air-cooled cast

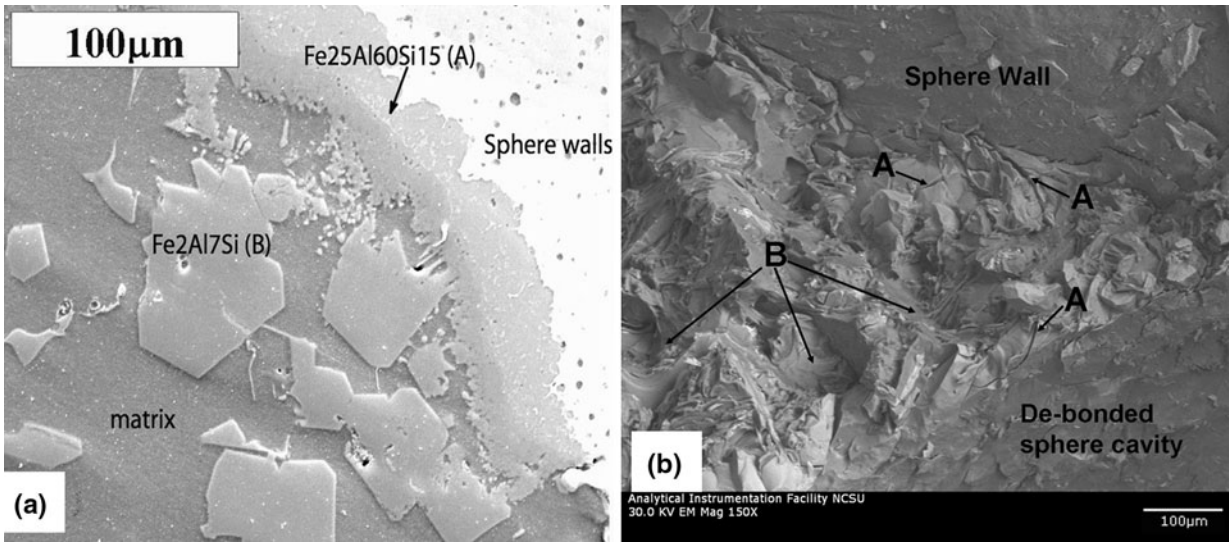

Fig. 4—Scanning electron microscopy (SEM) images of (*a*) intermetallic phases present in an Al-LC steel air-cooled cast sample[6] and (*b*) fracture surface of an Al-LC steel air-cooled cast sample after loading to failure under 4-point bending.

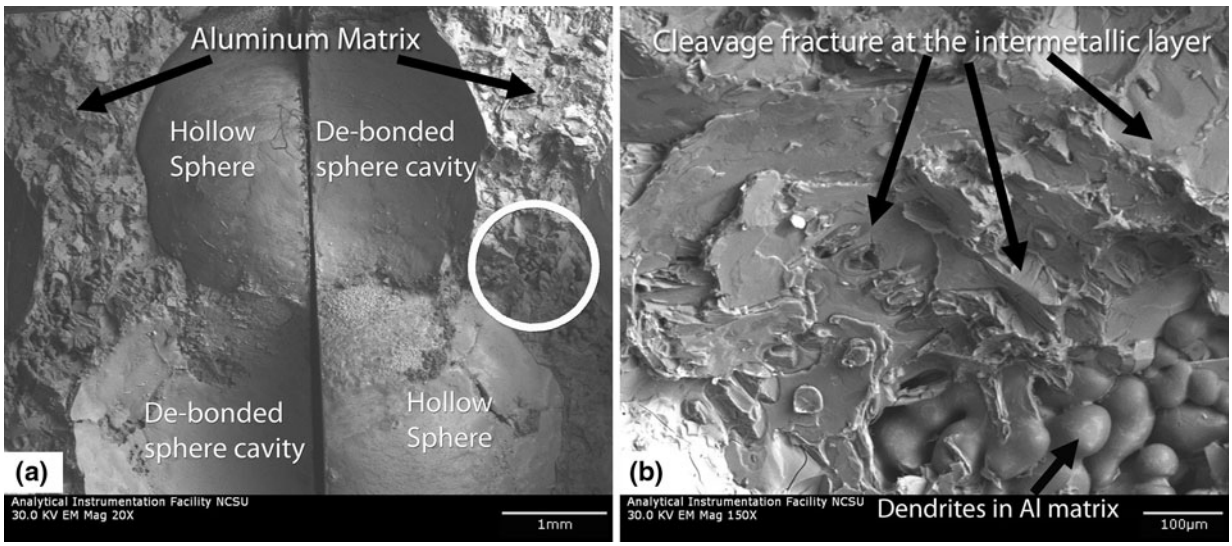

Fig. 5—SEM images of (*a*) matching fracture surfaces of an Al-SS air-cooled cast sample after loading to failure under 4-point bending and (*b*) enlargement of the circled area showing brittle fracture of intermetallic phases and dendrite structures present in the matrix.

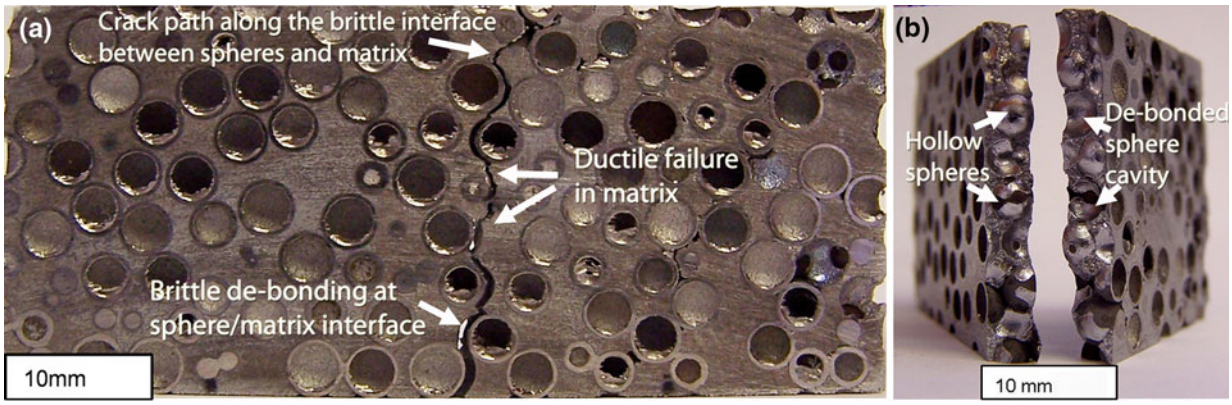

Fig. 6—Digital images of a failed cast Al-SS foam sample processed with air cooling (*a*) the top surface shows the crack propagation from intermetallic layer to intermetallic layer and (*b*) fracture surfaces showing how spheres pull out from the matrix.

sample, which shows a similar cracking pattern with the addition of dendrite formation present in the matrix. Dendrites were also found in the matrix of the Al-SS water-cooled composite foam but were not observed in the Al-LC steel foam.

The ultimate failure of cast samples resulted from the de-bonding of spheres from the matrix as shown in Figure 6. In many cases, parts of the intermetallic layer remain bonded to the sphere surfaces, whereas the rest of it layer remains in the trace of sphere left on the matrix. This indicates that the failure initiates within the intermetallic layer, and such a failure sequence is supported by the SEM fracture surface images. Figure 4(b) shows clear brittle cracking in the intermetallic layer surrounding the spheres (region A) as well as dimple-shaped formations in the matrix resulting from ductile failure (region B). It can also be noted that the brittle cracks are confined to the intermetallic layer and do not extend far from the sphere walls, which indicates that the ductile matrix has the effect of blunting the crack tip and slowing down the ultimate failure of the sample.

The AE events observed in real time during the test can be correlated to the failure features found in the postmortem SEM images and provide additional information about the sequence in which complete failure occurs. All cast samples showed a high number of AE events per cross-sectional area during the bending tests as shown in Figure 2. The events occurring before the yield point of the samples were mostly of low amplitude (less than 75 dB). Because these events occurred before the sample began to fail, it is concluded that they resulted from micromotion of the spheres under the elastic deformation of the matrix. Some localized plastic deformation may also occur during this phase and produce low amplitude AE events.

In the region between the yield stress and the maximum stress, several sharp, higher amplitude events up to 95 dB for both air- and water-cooled Al-SS samples and up to 90 dB for Al-LC samples occurred in addition to the continuation of the lower amplitude AE events. In general, it is accepted that higher amplitude AE events correspond to more brittle modes of cracking, whereas ductile failures produce AE events with lower amplitudes.[19] Consequently, these higher amplitude events can be related only to the isolated microcracking of the brittle intermetallic phases present in the sample, such as those found at the intermetallic interface layer (region A) in Figure 4(b). As loading continued past maximum stress, the individual microcracks initiating at the intermetallic phases propagated through the matrix to connect with other microcracks in nearby intermetallic regions. This process ultimately produces a macroscopic crack in the material that follows a path from intermetallic layer to intermetallic layer at the interfaces between spheres and matrix (Figure 6). Several AE events of both high and low amplitude continued after the maximum stress until the sample completely failed as the continual initiation of new microcracks and the coalescence of the existing microcracks formed the macroscopic crack that propagated completely through the sample thickness. Because of the plastic deformation of the sample at this stage, some of these events found after maximum stress were most likely caused by noise from the shifting of the sample in the jig, and as a result, the number of events occurring after maximum stress is not particularly revealing about the failure mechanisms.

Although this general failure behavior was observed in all cast samples, some differences were found in the total number of events and the amplitude distributions between the air-cooled and water-cooled Al-SS and the Al-LC steel foams because of variations in composition, size, and distribution of the intermetallic compounds. In cases of other composite materials containing brittle secondary phases, such as particle-reinforced metal matrix composites, it has been shown that the number of AE events observed is related to the degree of ductile failure found in the sample, as a more ductile failure results in more widely spread AE signals in the larger plastic zone.[24] This type of behavior is also observed in cast CMFs processed by various routes, in which the number and amplitude distribution of the AE events is related to the degree of ductility found in the sample. A larger plastic zone in cast CMF will cause a greater number of intermetallic regions to experience microcracking, consequently creating a larger number of AE events.

As shown in Figure 2, the Al-SS foam processed with the air-cooling method shows the most brittle failure and has the lowest maximum stress. The stress-displacement curve of these samples showed no plastic deformation region between yield and maximum stress, and the yield point calculated by the 0.2 pct offset method was close to the maximum stress value (Figures 2 and 3). This mostly brittle stress-displacement response is directly related to high amplitude AE events (corresponding to crack initiation in the intermetallic phases) that begin at stresses near 40 MPa before the yield point is reached. The air-cooled Al-SS foam showed the greatest number of high-amplitude events occurring before yield of any cast samples, reflecting its faster, more brittle failure.

Compared with the air-cooled Al-SS samples, the brittle intermetallic layer surrounding the sphere walls is considerably smaller in the Al-SS water-cooled samples.[18] This difference is reflected in both the mechanical behavior and the acoustic emission observed. Water-cooled Al-SS samples show a small region of plastic deformation between the yield point and the maximum stress, and the acoustic emission events with higher amplitudes begin when the stress is about 50 MPa. This result indicates that the smaller size of intermetallics in the water-cooled samples allows higher stresses to be sustained before a macroscopic crack completely connects through the sample to cause failure. In the mean time, the fast and more brittle failure in air-cooled Al-SS samples causes a smaller plastic zone that eventually causes a lesser number of total AE events/cross-sectional area compared with water-cooled Al-SS samples with more plastic deformation prior to failure.

The Al-LC steel samples (air-cooled) exhibited the most ductile behavior of the cast samples and also showed the most AE events/cross-sectional area reflecting the large plastic zone present in these samples. Al-LC steel samples reached maximum stresses of more than 80 MPa and showed a distinct region of plastic deformation between the yield point and the maximum stress. Acoustic emission of these samples also reflects their more ductile failure behavior in both the greater number of events and in their corresponding amplitude distribution. Unlike the Al-SS samples, none of the events before the yield point in Al-LC steel samples were high amplitude. Between yield and maximum stress, some higher amplitude events were observed, but the event amplitude gradually increased with increasing stress, and the highest amplitude ranged around 90 dB occurring at the maximum stress. This finding is in contrast to the Al-SS samples that consistently saw events up to 95 dB beginning at or before the yield point. Although the crack propagation follows the same pattern from intermetallic layer to intermetallic layer at the sphere-matrix interface, this lack of high-amplitude events implies that the failure mechanisms of the intermetallic layers in the Al-LC steel foam are more ductile under bending loads and the sample can sustain considerably higher stresses before microcracks in the intermetallic phases begin to form.

The varying degrees of ductility between the Al-LC steel and the Al-SS CMFs and the corresponding AE behaviors can be attributed to the differences in composition of the intermetallic phases. Elemental compositions of the intermetallic phases were obtained by SEM with energy dispersive X-ray spectroscopy in previous work for the three types of cast samples.[10,18] In general, intermetallics in the Al-LC steel foam have more iron content than intermetallics in the Al-SS foams because of the higher Fe content of the LC steel spheres. Also, the intermetallics of the Al-SS foams have some percentages of Ni and Cr that diffused from the SS spheres that are not present in the Al-LC steel composite foam.

The mechanical properties observed in other intermetallic systems including Al, Ni, Cr, and Fe suggest that the failure of intermetallics between Al-Ni and Al-Cr are more brittle than those between Al-Fe.[25] The yield strength of Ni-Al (50 pct-50 pct) intermetallics is generally lower than Fe-Al (~75 pct to 25 pct) intermetallics, and the same was found for these intermetallics when Cr was added in small amounts.[26] Also, it has been shown that the ductility of some binary Ni-Al systems can be improved by adding or increasing the percentage of a third element, particularly a transition metal such as Fe.[25]

These trends suggest that the presence of alloying elements in the intermetallic phases of Al-SS cast samples (in particular Ni) has made these intermetallics more brittle and resulted in a more brittle failure in both air and water-cooled Al-SS samples compared with Al-LC samples. This more brittle failure in the intermetallic phases of the Al-SS foams is reflected even more by the AE of higher amplitudes in the crack initiation and propagation phases before the maximum stress is reached. In addition, the more equiaxed grains with no dendrite formation observed in the Al-LC composite foam may also contribute to its greater ductility. The differences in composition and distribution of intermetallic phases, microstructure morphology, and the corresponding failure mechanisms between the Al-SS and Al-LC cast foams are currently being studied in more detail.

B. *Powder Metallurgy (PM) Samples*

Unlike the cast samples, CMF samples processed by PM methods are made from similar materials and have no intermetallic compounds. As shown in Figure 2, both the LC and SS PM samples show much more ductile behavior with clearly visible regions of plastic deformation between the yield point and the maximum stress. The deformation of the PM samples was also much slower and the bending jig rollers slipped out of contact with the sample before the crack had fully propagated through the entire sample thickness, leaving the upper surface still intact even after full loading as shown in Figure 7.

Figure 8 shows SEM images from the matching fracture surfaces of a PM-LC steel sample (Figure 8(a)) as well as the porosities that exist within the sphere walls and the matrix (Figure 8(b)). In the figure, the hollow spheres are indicated with "HS" and the corresponding depression left by the debonded sphere on the other

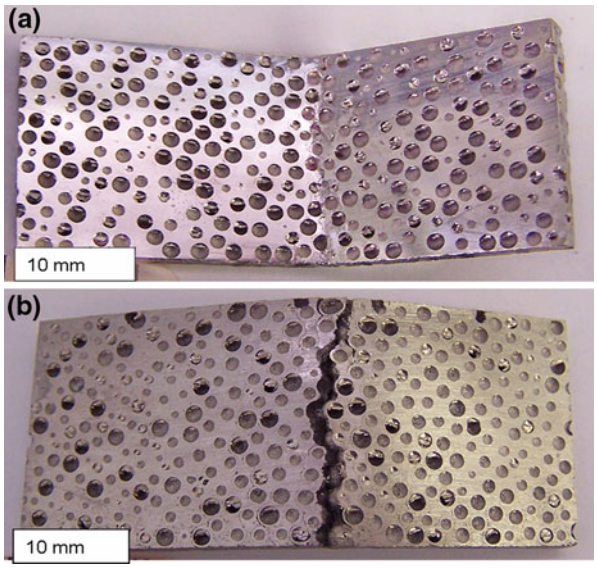

Fig. 7—Digital images of a failed PM SS sample under 4-point bending test showing the sample as one piece even after full loading: (*a*) upper surface and (*b*) lower surface.

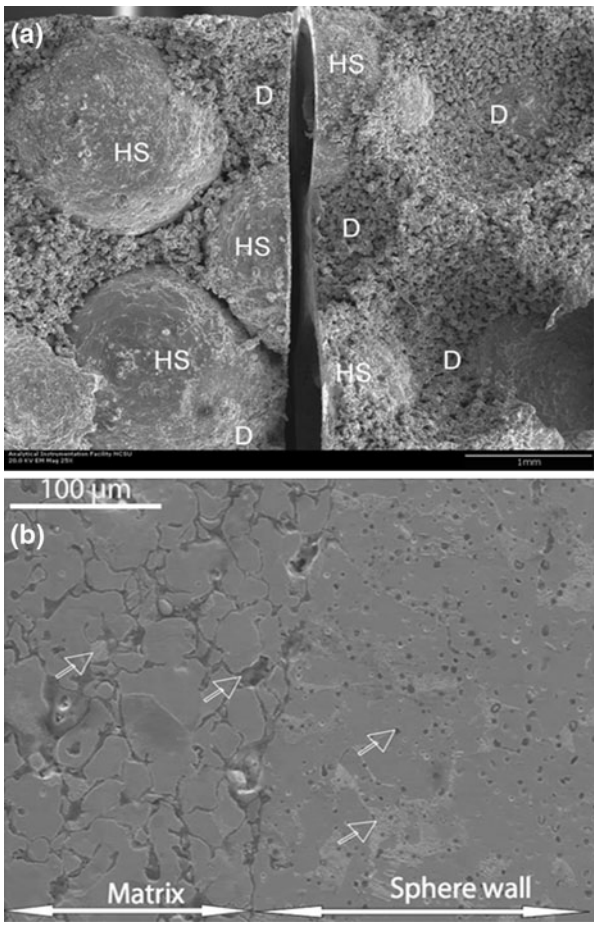

Fig. 8—(*a*) SEM images of the matching fracture surfaces of PM-LC steel CMF after 4-point bending test where HS indicates hollow sphere and D indicates a depression left by a debonded sphere. (*b*) SEM image showing preexisting porosities (highlighted by arrows) in the matrix and sphere walls.[7]

surface of the sample is indicated with "D". As can be observed from the SEM images, the primary failure mechanisms in the PM samples are related to plastic deformation of the matrix and breaking ligaments between preexisting microporosities in the matrix followed by eventual debonding of the spheres from the matrix. The fracture surfaces of the PM-SS samples showed similar features, and it can be concluded that the same failure mechanisms govern both types of PM CMF.

The ductile type of failure observed in PM foams produces much less acoustic emission than shown in the cast samples, with approximately one event per cross-sectional area (Figure 2). Since the matrix of the PM CMF is fairly homogenous in nature with only some porosities and no intermetallic phases, the large plastic zones present in the ductile failure of these samples do not cause any increase in the number of AE events. Consequently, large amounts of AE, such as that generated by micro-cracking in the intermetallic regions of cast samples, are not seen here.

Also, none of the events in the PM samples occurred before the yield point was reached, indicating that no substantial localized plastic deformation is occurring in the sample during the linear elastic region. Some slight shifts of microporosities in the matrix might occur during this time, but any AE produced by that was too small to be detected above the threshold level of 30 mV. In addition, all the AE events observed in both LC and SS PM samples had amplitudes less than 75 dB, which indicated that the deformation causing these events is occurring in a ductile manner that does not produce any sharp, high-amplitude AE signals that are characteristic of a brittle failure. The few events that did occur after the material had begun to deform plastically likely resulted from the spheres shifting and becoming debonded from the matrix. The presence of only a few events that are all low amplitude reflects a complete ductile failure mechanism that characterizes the PM CMFs.

C. *Reliability of Results*

To verify the accuracy of our bending test results on thin samples, the yield and maximum strength of each sample is compared with the yield and plateau strength from monotonic compression tests conducted on thicker samples with at least 7–8 spheres on each side (Figure 9). The details of the monotonic compression test procedure, results and discussion can be found elsewhere.[10,11,27]

As can be observed in Figure 9(a), the yield strength of each sample under bending and monotonic compression is essentially in the same range. Because the stress/strain behavior observed during bending tests is consistent with the compressive behavior of larger samples up to the yield point, it can be concluded that size effects caused by small bending sample thickness are minor, and the behavior observed is still a reasonably accurate representation of bulk CMF properties.

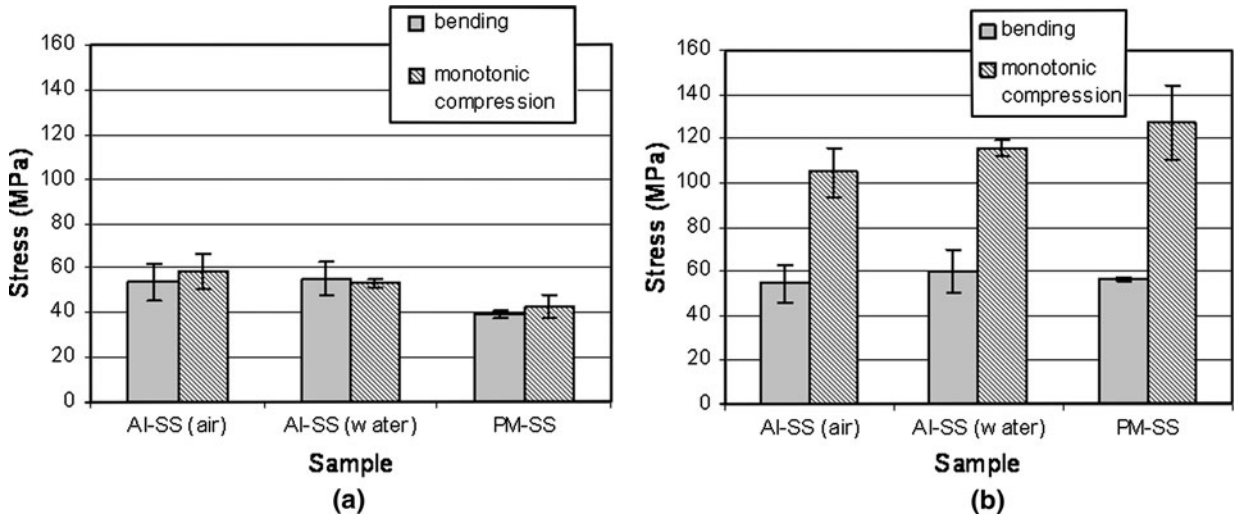

Fig. 9—Comparison of (*a*) bending sample yield strength with compressive yield strength and (*b*) maximum strength under bending with compressive plateau strength.

It is notable that bending samples experience both compression and tension during loading and metal foams are known to have lower strength in tension than compression,[1] particularly at higher stresses above the yield point. This point can be better observed in a comparison between the ultimate bending strength of foam samples and their compression plateau strength presented in Figure 9(b). A consistent 50 pct increase observed in the CMF plateau strengths under compression loading compared with the ultimate strength of thinner samples under bending is caused by the component of tension present in the bending samples, which is another reason to believe that the mechanical properties characterized in this study are reasonable representations of bulk properties of CMFs.

IV. CONCLUSIONS

CMFs produced by both casting and PM techniques show favorable performance under bending loads. The acoustic emission signals detected during the bending tests were explained by the failure mechanisms that occur within the samples and are correlated to the features observed on the fracture surfaces using SEM. The presence of intermetallic compounds in the cast samples results in a high amount of AE activity related to brittle failure in intermetallic phases, but the ductile matrix sufficiently blunts these initial cracks and allows the sample to sustain high stresses. The PM samples have no intermetallic compounds and exhibit completely ductile behavior with much less acoustic emission. Consistency between the results collected from bending tests on thinner samples compared with those collected from monotonic compression tests on thicker samples confirmed the reliability of the results.

ACKNOWLEDGMENTS

The authors acknowledge the National Science Foundation for funding this research through Award (#0238929) as well as the support for a student to conduct research at The University of Tokyo through the IREE supplement #0738423. Also, the authors acknowledge Dr. Manabu Enoki and his research team at The University of Tokyo for being generous hosts to the student. In addition, the authors would like to acknowledge Stefan Sandukas and Justin Williams for their assistance with sample preparation and SEM fractography.

REFERENCES

1. M.F. Ashby, A. Evans, N.A. Fleck, L.J. Gibson, J.W. Hutchinson, and H.N.G. Wadley: *Metal Foams: A Design Guide*, Butterworth-Heinemann, Wolburn, MA, 2000, pp. 3–61.
2. H.P. Degischer and B. Kriszt: *Handbook of Cellular Metals, Production, Processing, Applications*, Wiley-VCH Verlag GMBH, Weinheim, Germany, 2002, pp. 127–236, 355–59.
3. Y. Sugimura, H. Meyer, M.Y. He, H. Bart-Smith, J. Grensted, and A.G. Evans: *Acta Mater.*, 1997, vol. 45, pp. 5245–59.
4. H. Bart-Smith, A.F Bastawros, D.R. Mumm, A.G. Evans, D.J. Sypeck, and H.N.G. Wadley: *Acta Mater.*, 1998, vol. 46, pp. 3583–92.
5. U. Ramamurty and A. Paul: *Acta Mater.*, 2004, vol. 52, pp. 869–76.
6. I. Jeon and T. Asahina: *Acta Mater.*, 2005, vol. 53, pp. 3415–23.
7. A.E. Simone and L.J. Gibson: *Acta Mater.*, 1998, vol. 46, pp. 3109–23.
8. D.L. McDowell, T.-J. Lim, and B. Smith: *Acta Mater.*, 2002, vol. 50, pp. 2867–79.
9. D.M. Kupp, T.D. Claar, G. Stephani, and U. Waag: *Proc. Adv. Powder Metall. Part. Mater.*, New Orleans, LA, 2001, pp. 1486–94.
10. L.J. Vendra and A. Rabiei: *Mater. Sci. Eng. A*, 2007, vol. 465, pp. 59–67.
11. B.P. Neville and A. Rabiei: *Mater. Des.*, 2008, vol. 29, pp. 388–96.
12. A. Rabiei, B. Neville, N. Reese, and L. Vendra: *Mater. Sci. Forum*, 2007, pp. 1868–73.
13. A. Rabiei, L. Vendra, N. Reese, N. Young, and B.P. Neville: *Mater. Trans.*, 2006, vol. 47, pp. 2148–53.

14. A. Rabiei and A.T. O'Neill: *Mater. Sci. Eng. A*, 2005, vol. 404, pp. 159–64.
15. A. Rabiei, A.T. O'Neill, and B.P.S Neville: *Mater. Res. Soc. Symp. Proc. Process. Devel. New High Strength Metal Foam Mater. Space Appl.*, 2005, vol. 851, pp. 517–26.
16. L.J. Vendra and A. Rabiei: *Mater. Sci. Eng. A*, 2010, vol. 527, pp. 1784–90.
17. A. Rabiei and L. Vendra: *MetFoam 2007-Proc. 5th Int. Conf. Porous Metals Metall. Foams*, 2007, pp. 387–90.
18. L.J. Vendra: Ph.D. Dissertation, North Carolina State University, Raleigh, NC, 2008.
19. P. Kalyanasundaram, C.K. Mukhopadhyay, and S.V. Subba Rao: *Practical Acoustic Emission*, Alpha Science International Ltd., Oxford, UK, 2007, pp. 1–136.
20. C.U. Grosse and L.M. Linzer: in *Acoustic Emission Testing*, C.U. Grosse and M. Ohtsu, eds., Springer-Verlag, Berlin, Germany, 2008, pp. 64–65.
21. K. Ito and M. Enoki: *Mater. Trans.*, 2007, vol. 48, pp. 1221–26.
22. N.Ohisa and T. Kishi: *Proc. 1982 Joint Conf. Exper. Mech., Soc. Exper. Stress Anal.*, 1982.
23. Data sheet for Alporas, Shinko Wire Company, Ltd., www.shinko-wire.co.jp/product/alporas-eng.pdf, 2008.
24. A. Rabiei, B.-N. Kim, M. Enoki, and T. Kishi: *Scripta Mater.*, 1997, vol. 37, pp. 801–08.
25. C.L. Briant: in *Intermetallic Compounds: Basic Mechanical Properties and Lattice Defects of Intermetallic Compounds*, J.H. Westbrook and R.L. Fleischer, eds., John Wiley & Sons, Ltd., West Sussex, UK, 2000, pp. 25–40.
26. J. Payne and D.D. Pramod: *Properties of Intermetallic Alloys*, Purdue Research Foundation, West Lafayette, IN, 1994, pp. 8.30–8.35, 8.72, 11.8–11.20, 11.165–11.167.
27. B.P. Neville: Ph.D. Dissertation, North Carolina State University, Raleigh, NC, 2006.